Spin Modulation of Spectrally Broadened VLF Signals

H. G. JAMES

Communications Research Centre, Ottawa, Ontario, Canada

T. F. BELL

Space, Telecommunications and Radioscience Laboratory, Stanford University, Stanford, California

The spectra of broadened VLF signals from ground transmitters received on the spinning ISIS spacecraft have a characteristic temporal dependence when the long receiving dipoles pass close to parallel to the earth's magnetic field direction. As the angle between the dipole and the field direction passes its minimum, the spectra evolve from having enhanced negative Doppler components to having enhanced positive Doppler components or vice versa. The relative orientation of the spin, spacecraft velocity, and magnetic field vectors determines whether the enhancement evolves from positive to negative Doppler or from negative to positive. Theoretical calculations of the Doppler spectra agree with observations from the ISIS spacecraft. These analyses show that wave vectors corresponding to broadened spectra are confined to a narrow range of azimuths about the magnetic field direction. The wave vectors are distributed through a range of polar angles with respect to the magnetic field direction, possibly as the result of scattering of the upcoming waves in the ionosphere below the spacecraft. The technique has been used to deduce the preferred azimuth in the case of one spectrum.

1. INTRODUCTION

Spectral broadening of VLF signals from ground transmitters has been observed on the ISIS I, ISIS II, ISEE 1 and DE 1 spacecraft [*Bell et al.*, 1983, 1985; *Inan and Bell*, 1985] and on the Aureol 3 and IK 19 spacecraft [*Tanaka et al.*, 1984; *Titova et al.*, 1984a, b, c]. Upgoing signals in the frequency range 10–20 kHz with initial bandwidths of about 1 Hz experience a bandwidth increase of up to 1 kHz as they propagate into the topside ionosphere. In some cases, the spectral intensity is lower at the transmitter carrier frequency than at shifted frequencies on the shoulders of the spectrum. Broadened spectra are observed on downcoming whistler-mode waves that have been reflected from the conjugate point [*Bell et al.*, 1983].

The explanation of broadening may be important for the interpretation of whistler-mode signals in the ionosphere and magnetosphere, whether these signals are observed on the ground or in space. Whistlers, artificial signals, and downcoming emissions from natural sources all may be broadened and amplified by one mechanism. Quantitative explanations of the energetics of such signals may need to include the spectral-broadening mechanism as a first-order effect.

More than one physical process has been invoked to explain VLF spectral broadening. *Bell et al.* [1983] described "apparent" broadening: All waves measured are at the carrier frequency of the ground transmitter. A distribution of quasi-electrostatic wave vectors directed close to parallel to the resonance cone surface is deduced. Consequently, large Doppler shifts with respect to the carrier frequency occur in the signal received by a moving spacecraft. *Hoc and Bell* [1985] attribute the wave vector distribution to scattering by field-aligned slabs of depleted or enhanced ionization.

An explanation based on nonlinear scattering has also been proposed. Broadening is associated with precipitating elec-

trons [*Bell et al.*, 1983]. This free energy source could change the wave vector distribution. *Titova et al.* [1984a] have proposed a scheme of nonlinear scattering which results in an output signal with a true, not apparent, shift from the carrier frequency. Thus the observed shifts of spectral components could be the sums of such "true" shifts of the output wave frequency from the carrier plus the "apparent" shifts due to the Doppler effect.

This paper deals with an observational technique that was developed to help in evaluating scattering theories. The present analysis deduces wave electric vector distributions from the time variation of the observed spectra of ground transmissions. The establishment of the electric vector distribution, both in polar and azimuthal angles, may indicate the type and location of the scattering process that produced it.

The physical source of spin modulation is explained in section 2. The theoretical consequences of specific electric vector distributions founded on the ideas of *Bell et al.* [1983] are discussed therein. Section 3 compares observations with theory. The principal result of this is to show the superiority of the assumption of a restricted azimuthal range for the electric vectors in a few observed cases and to illustrate how a preferred azimuth was deduced in one case.

2. SPIN MODULATION

2.1. Basic Signature

The spectral breadth of transionospherically propagated VLF signals is often of the order of a few hundred hertz. Doppler shifts of this magnitude correspond to whistler-mode waves whose wave vectors are close to parallel to the resonance cone. The wave vector $\vec{k}$ of such quasi-electrostatic waves are virtually parallel to their corresponding electric fields $\vec{E}$. For frequencies and plasma conditions encountered in this study, $\vec{E}$ and $\vec{k}$ are within a few degrees of perpendicular to the terrestrial magnetic field $\vec{B}_0$.

ISIS data surveys indicate that the "cartwheel" spin mode is necessary for the observation of the spin modulation. In this mode the spacecraft spin vector is within a few degrees of
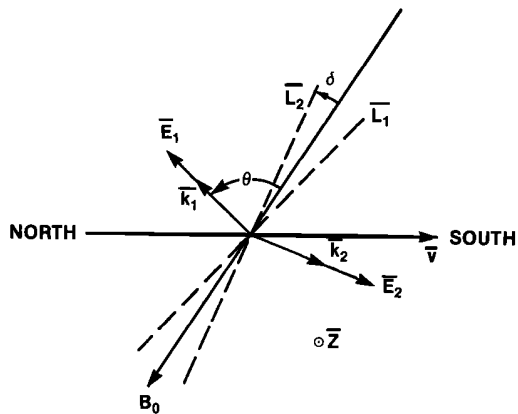
Fig. 1. Relation of quasi-electrostatic wave $\bar{E}$ fields, $\bar{E}_1$, and $\bar{E}_2$ to the earth's magnetic field $\bar{B}_0$, the spacecraft spin vector $\bar{Z}$, the spacecraft velocity $\bar{v}$, and two positions, $\bar{L}_1$ and $\bar{L}_2$, of the rotating dipole antenna. $\bar{E}_1$ produces a positive f_D and $\bar{E}_2$ a negative f_D.

perpendicular to the orbital plane. For polar-orbiting spacecraft the orbital plane is close to the magnetic meridian except at high latitudes. Hence the receiving dipole, deployed in the spacecraft equatorial plane, rotates approximately in the magnetic meridian plane.

The resultant effect on the received signals can be explained with reference to Figure 1. For purposes of preliminary discussion, consider the simple situation in which $\bar{B}_0$ and the satellite velocity vector $\bar{v}$ both lie in the dipole spin plane. $\bar{E}$ is also assumed to be exactly parallel to $\bar{k}$. Suppose that there are two incoherent waves with vectors $\bar{k}_1$ and $\bar{k}_2$ in the aforementioned plane, on opposite sides of $\bar{B}_0$. The variable θ is the angle between $\bar{k}$ and $-\bar{B}_0$. The spin vector $\bar{Z}$ is assumed straight out of the page with the result that the angle δ between the dipole vector $\bar{L}$ and $-\bar{B}_0$ sweeps all values in 0°–360°.

Two dipole orientations of interest, $\bar{L}_1$ and $\bar{L}_2$, are shown in Figure 1. At $\bar{L}_1$ the dipole is exactly perpendicular to $\bar{E}_1$ and hence no signal is received from that component, while some signal is received from the $\bar{E}_2$ component. A short while later the dipole has passed $\delta = 0°$ and is now at $\bar{L}_2$, where it discriminates against the reception of the $\bar{E}_2$ component.

The Doppler shift f_D of component 1 is $-\bar{k}_1 \cdot \bar{v}/2\pi$. In the above sequence the $\bar{k}_1$ wave (positive f_D) is suppressed and then the $\bar{k}_2$ wave (negative f_D) is suppressed.

The usual form of a broadened VLF spectrum is a continuous distribution of signal power $P_D(f_D)$ for all f_D in $-100 \gtrsim f_D \gtrsim 100$ Hz. Except for magnitudes less than a few hertz, all f_D in that range correspond to $\bar{E}$ very close to the resonance cone. Qualitatively, the effect of a set of $\bar{E}$ vectors distributed through a range of θ on each side of the magnetic field is the same as for Figure 1. At orientations like $\bar{L}_1$ the positive Doppler components are reduced, and at orientations like $\bar{L}_2$ the negative components are reduced.

The spin modulation of the received signal is determined in part by the variation of the antenna impedance and directional gain as functions of the angle δ. Most of the wavelengths analyzed are much longer than the ISIS dipole antenna length. It is assumed that the intensity gain of a short dipole varies as the square of the cosine of the angle between the electrical field and the antenna, $\theta - \delta$. The cold plasma theory for the dipole impedance predicts modest changes for δ near 0° and small changes in impedance at other values of δ.

2.2. Geometrical Asymmetry

Generally, the principal vectors $\bar{v}$, $\bar{B}_0$, $\bar{E}$, and $\bar{Z}$ have a more complicated disposition than in Figure 1. Even in Figure 1, the fact that $\bar{v}$ is not at 90° to $\bar{B}_0$ produces some asymmetry: When $\bar{L}$ is perpendicular to $\bar{k}_2$, the Doppler shift $f_D = -\bar{k}_1 \cdot \bar{v}/2\pi$ has a different magnitude from the opposite case $f_D = -\bar{k}_2 \cdot \bar{v}/2\pi$, even for $|\bar{k}_1| = |\bar{k}_2|$.

The orientation of the dipole spin plane with respect to the plane of an assumed planar $\bar{E}$ distribution is important to this study. In real cases, the spacecraft spin causes δ to pass through a minimal $\delta = \delta_{min} \neq 0$. The time at which $\delta = \delta_{min}$ is generally different from the time midway between $\bar{L}$ closest to $\bar{k}_1$ and $\bar{L}$ closest to $\bar{k}_2$. It will be shown that in the case of a planar $\bar{E}$ distribution, the detailed shape of the received spectrum when δ is near δ_{min} is dependent on the azimuth of the $\bar{E}$ distribution.

The orbit-normal vector is perpendicular to the orbital plane and has a direction defined in the right-handed spin vector sense. It turns out that the angle between the satellite spin vector and the orbit-normal vector uniquely determines the sign of the slope of the characteristic spectral signature near δ_{min}. This holds for both north-bound and southbound passes in both hemispheres. When the angle is about 180°, as it always is in ISIS II "cartwheel" data, the negative f_D components are first stronger, and then the positive f_D. The result on a frequency-time plot is an "upturn" signature. Examples are given later in this article. When the angle is near zero, the spectra change from enhanced positive f_D to enhanced negative f_D.

2.3. Computation of Spin Modulation

Two different distributions of incoherent $\bar{E}$ vectors have been used as the basis for a theoretical calculation of spin modulation: $\bar{E}$ vectors distributed over a range of θ at a given azimuth ϕ and $\bar{E}$ vectors distributed in both θ and ϕ. For a definition of angles see Figure A1.

Bell et al. [1983] analyzed the case of wave vectors confined to one azimuth ϕ. In a cold plasma the differential power flux distribution with respect to θ, $\partial S/\partial \theta \equiv G$, is related to the differential power distribution with respect to Doppler frequency f_D, $\partial p/\partial f_D \equiv P_D$ through [see Bell et al. [1983], equations (A3), (A11)]

$$P_D(f_D, \bar{L}) = \frac{CF_D(\theta, \bar{L}, \phi)}{n(\theta)F_\theta(\theta)(\partial f_D/\partial\theta)} G(\theta) \qquad (1)$$

Here C is a constant. G is identical to P_θ of Bell et al. [1983]. F_D is a proportionality factor which can be derived from the cold plasma theory and which allows the power into the receiver to be expressed in terms of the wave $\bar{E}$ vector components and the antenna vector $\bar{L}$. The azimuth ϕ is the angle between the plane of wave vectors and the plane defined by $\bar{B}_0$ and $\bar{v}$. The parameter $n(\theta)$ is the refractive index and is evaluated at the carrier frequency. $F_\theta(\theta)$ is also derivable from cold plasma theory and relates the differential power flux G to the $\bar{E}$ vector. The differential $\partial f_D/\partial\theta$ depends on θ, ϕ, and $\bar{v}$ and is henceforth denoted $F_3(\theta, \phi, \bar{v})$. The variables F_D and n both depend on the dielectric tensor whose components, in the present case, have been evaluated for electrons and one type of ion (either H^+ or O^+).

2.3.1. Range of azimuths. When $\bar{E}$ vectors are distributed through both azimuth ϕ and polar angle θ, it is necessary to cast (1) in a more general form. If there are j azimuths, each
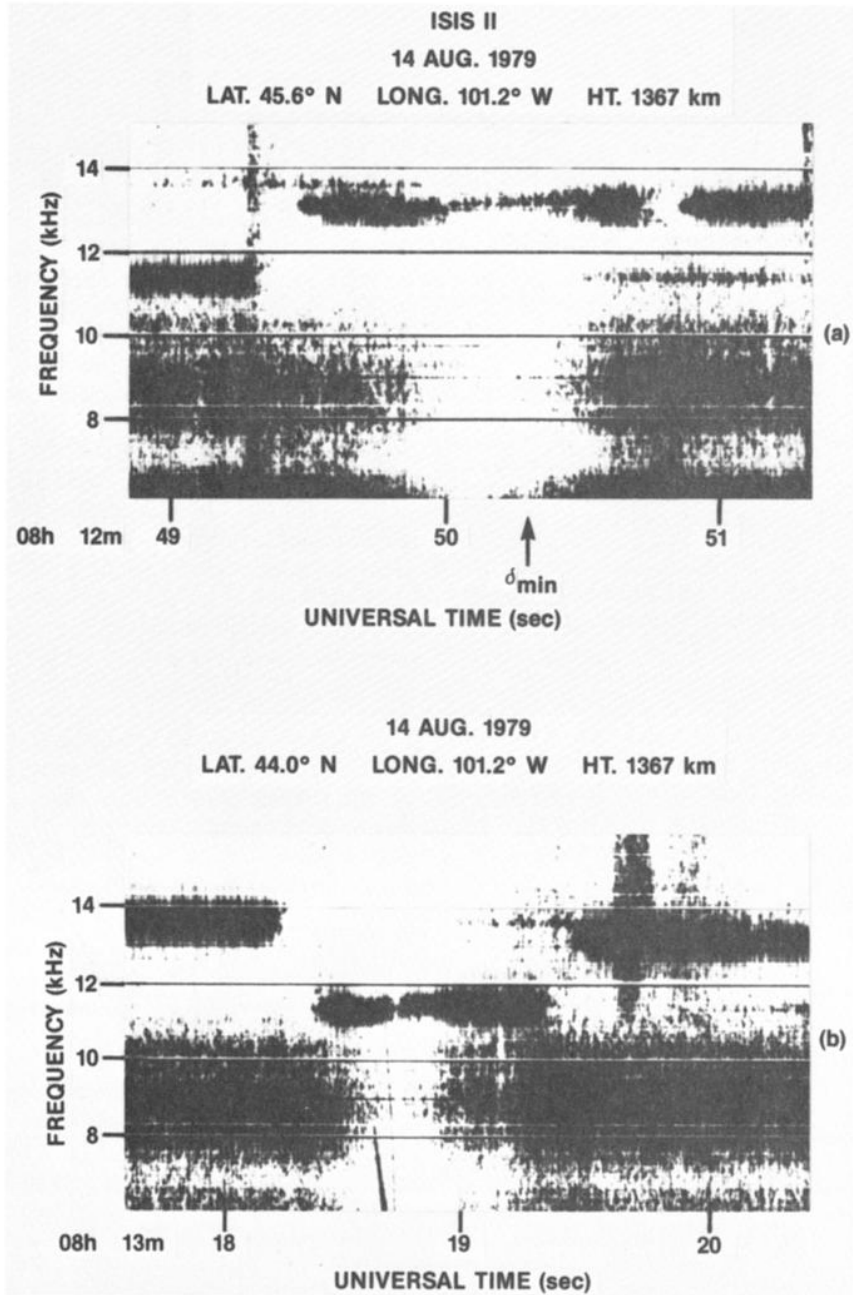
Fig. 2. Frequency-time-amplitude display of spectrally broadened transmissions from the OND transmitter. (a) The format includes a 1-s pulse at 11.3 kHz around 49 s and two 1-s pulses at 13.1 kHz starting at 49.5 s. The central 13.1-kHz pulse exhibits characteristic spin modulation near δ_{min}. (b) Pulses at 13.6, 11.3, and 13.1 kHz are shown. Both panels have a strong band of natural hiss in the 8- to 10-kHz range, also subject to spin modulation.

containing the same $G(\theta)$ distribution, then the total signal P_D is

$$P_D(f_D, \bar{L}) = C \sum_j \frac{F_D(\theta_j, \bar{L}, \phi_j)}{n(\theta_j) F_\theta(\theta_j) F_3(\theta_j, \phi_j, \bar{v})} G(\theta_j) \qquad (2)$$

There is a one-to-one correspondence between θ_j and ϕ_j for a given f_D through $f_D = -\bar{k} \cdot \bar{v}/2\pi$. This is evaluated in the Appendix. Equation (2) rewritten in differential form is

$$P_D(f_D, \bar{L}) = C \int \frac{F_D'(\bar{L}, \phi, f_D)}{n'(\phi, f_D) F_\theta'(\phi, f_D) F_3'(\phi, f_D, \bar{v})} R \, d\phi \qquad (3)$$

where R is the total differential $dG/d\phi$. The primed forms of the functions are what result from substituting in the corresponding unprimed functions in (2) for θ using the aforementioned definition of f_D.

In the present work the distributions G and R are unknowns. We demonstrate the ability of the model based on (1) to predict spin modulation patterns that are consistent with the observations. P_D near δ_{min} can be calculated directly from assumed forms of R or based on the observed P_D near $\delta = 90°$. This paper contains examples of the latter type of calculation. The Appendix describes assumptions and techniques for deconvoluting R from P_D.

ISIS II

14 AUG. 1979

LAT. 44.6° N   LONG. 101.2° W   HT. 1367 km

3 NOV. 1971

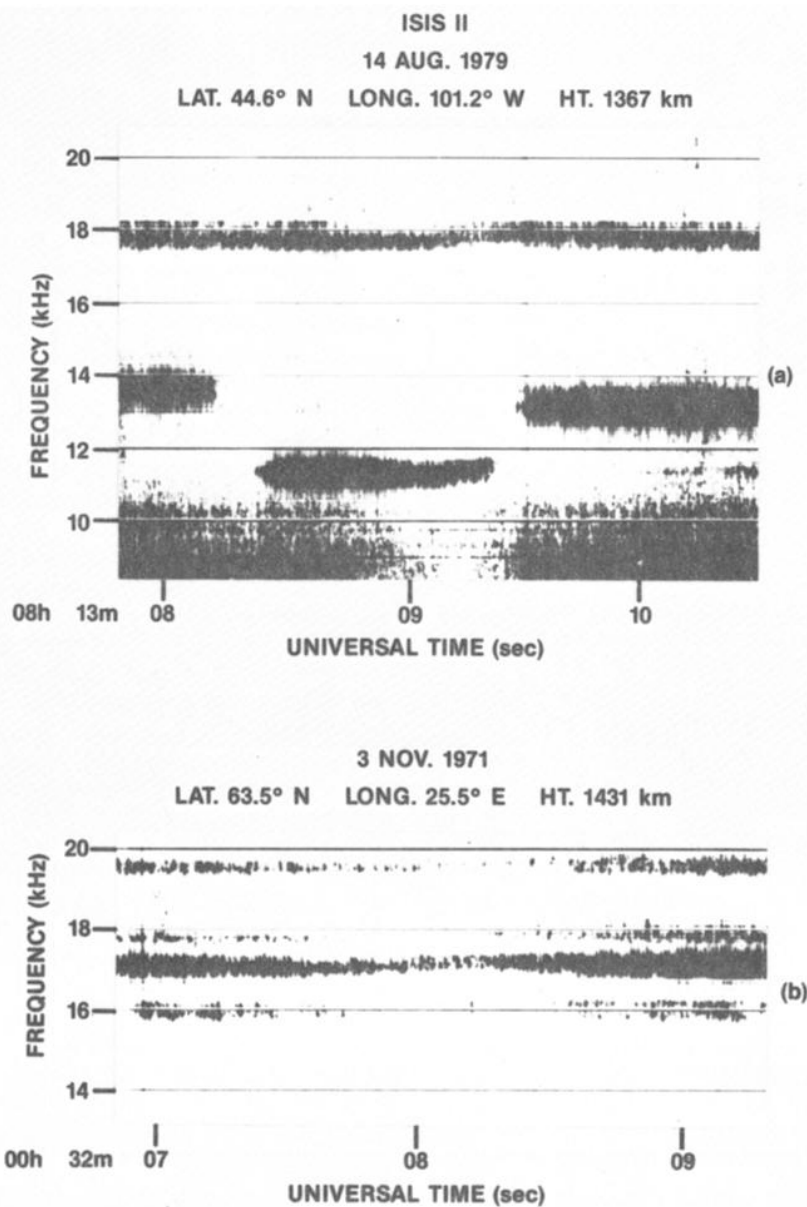LAT. 63.5° N   LONG. 25.5° E   HT. 1431 km

Fig. 3. Frequency-time-amplitude display of spectrally broadened VLF transmissions. (a) The central OND pulse at 11.3 kHz exhibits spin modulation effects between 9.0 and 9.5 s, as the does the NAA transmission at 17.8 kHz. (b) A group of continuous VLF transmissions in northern Europe. The strongest signals at 17.2 and 19.7 kHz have the characteristic upturn signature just after 8 s.

2.3.2. *Single azimuth.* The assumption that all $\bar{E}$ and $\bar{k}$ vectors are confined to one azimuth simplifies the calculation of the temporal evolution of P_D. The goal being to calculate P_D for δ near δ_{min}, there is no need to evaluate R explicitly in this case. The spectrum at general time t is

$$P_D(f_D, \bar{L}(t)) = \frac{F_D(\theta, \bar{L}(t), \phi)}{F_D(\theta, \bar{L}(t_0), \phi)} \, P_D(f_D, \bar{L}(t_0)) \qquad (4)$$

in which $\delta = 90°$ at t_0. Equation (A5) gives the ratio of the F_D on the right side of (4).

3. COMPUTATION OF $\bar{E}$ VECTOR DISTRIBUTIONS FROM ISIS DATA

3.1. *Observations*

The ISIS II spacecraft is in a circular orbit near an altitude of 1400 km with an inclination of 89°. Such an orbit has carried the satellite over a variety of ground VLF transmitters. For approximately 50% of the time the spacecraft has been in a cartwheel spin mode appropriate for the spin modulation of received signals. The signals of interest were received on the 73.2-m dipole and detected by the broadband (0–25 kHz) VLF receiver [*Franklin et al.,* 1968]. The dipole rotates in the spacecraft spin equatorial plane, and the spin rate is about 3 rpm.

Figures 2 and 3 illustrate spin modulation on different ground transmissions. Figure 2 contains examples from the August 14, 1979, pass near the Omega–North Dakota (OND) transmitter discussed by *Bell et al.* [1983]. The approximately 1-s long pulse at 13.1 kHz in Figure 2a exhibits the characteristic narrowing of signal spectral width accompanied by a rising slope, or upturn. The slope is also seen on the 11.3-kHz pulse in Figure 2b. The two data sets in Figure 2 are the subject of quantitative analyses in this paper.
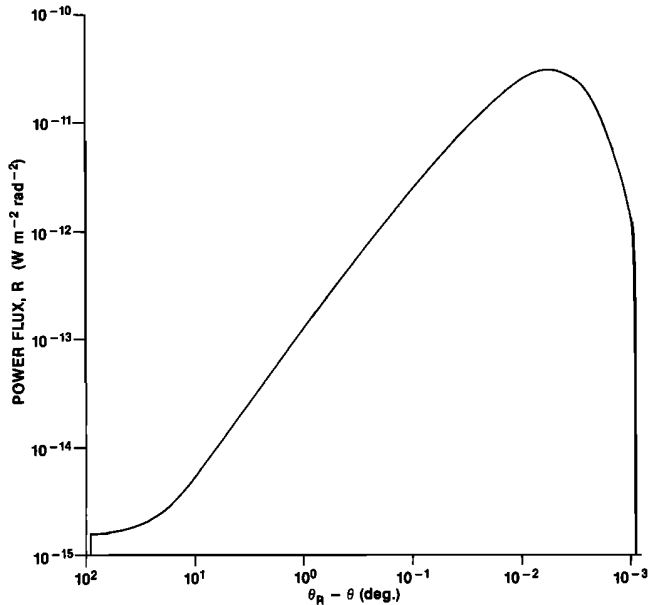
Fig. 4. Angular power distribution $R(\theta)$ resulting from deconvolution of the $P_D(f_D)$ spectrum observed near the time of Figure 2a, for $\delta = 90°$.

Broadened signals at 17.8 kHz from NAA, the U.S. Navy transmitter at Cutler, Maine, and at 11.3 kHz from OND provide evidence of the typical mild upturn signature at 9.0–9.5 s in Figure 3a. In Figure 3b the upturn is seen around 8 s on powerful unidentified transmissions at 17.2 and 19.7 kHz in the North European sector.

The ensemble of ISIS data surveyed indicated that the upturn signature is commonly obtained when necessary conditions are met: significant Doppler broadening as discussed by Bell et al. [1983], cartwheel orientation, signal strength sufficient to be detected at δ_{min}. Below, it will be shown that the frequent occurrence of the spin modulation signature in these and other passes supports the explanation of spectral broadening in terms of a distribution R with most of the power flux at $\hat{k}$ close to the resonance cone.

The ISIS II pass on August 14, 1979, produced some of the clearest cases of spin modulation, of which Figure 2 gives two examples. These two 1-s pulses have been analyzed using both the distributed and single-azimuth ϕ dependence.

Topside sounder data from passes at the same local time and location gathered within a few days of August 14, 1979, indicated an average plasma frequency $f_{pe} = 0.5$ MHz at the spacecraft. This is roughly consistent with f_{pe} determined independently from the lower-hybrid resonant frequency identified

as the frequency of the lower edge of broadband hiss [Bell et al., 1983]. Given an electron gyrofrequency of 0.9 MHz and a plasma presumed to consist of electrons and O^+ ions only, the resonance cone angle $\theta_R = 88.3°$ for a carrier frequency $f_0 = 13.1$ kHz.

3.2. Range of Azimuths

The distribution $R(\theta)$ was evaluated for the cases in Figure 2 using a commonly observed form for P_D at $\delta \simeq 90°$. Although some of the August 14, 1979, spectra selected by Bell et al. [1983] exhibit a suppression of the signal level near $f_D = 0$, this phenomenon is not always observed in spectrally broadened VLF. A spectrum of the form $P_{max} \exp (-f_D^2/f_w^2)$, with a half width $f_w = 150$ Hz, was chosen as the basis of analysis. A half width of 150 Hz is typical of spectra reported by Bell et al. [1983, Figure 11]. The central line spectrum intensity P_{max} is determined from observed ISIS received signal intensities.

The antenna orientation $\hat{L}$ was derived from magnetometer and solar sensor data routinely recorded. When compared with more careful determinations of attitude [McDiarmid et al., 1978], $\hat{L}$ was assessed an uncertainty of $\leq 2°$ in both the θ and ϕ directions as defined in Figure A1. The angle δ is determined directly from the ISIS magnetometers, and apart from considerations of antenna bending (see below), has an accuracy of about $0.1°$. The magnetic field $\vec{B}_0$ was computed using the International Geomagnetic Reference Field 1980 coefficient set [International Association of Geomagnetism and Aeronomy, 1986]. The inaccuracy of the satellite velocity $\vec{v}$, derived from the North-American-Air-Defense-supplied ephemerides, is negligible.

In the August 14, 1979, pass at 0813 UT, $\delta_{min} = 3.3°$ and the angle $(\vec{v}, -\vec{B}_0) = 72°$. The spin vector $\vec{Z}$ is very close to the $-y$ axis shown in Figure A1; when the long antenna passes through the x-y plane, it makes an angle of $4.5°$ with the x axis.

The evaluation of R from $P_D = P_{max} \exp (-f_D^2/f_w^2)$ as described in the first section of the Appendix leads to Figure 4. The numerical deconvolution of R in (2) assumed that propagation was distributed through all azimuths. A value of P_{max} corresponding to a typical open circuit voltage at spectral line center delivered by the antenna of $50\mu V/\sqrt{Hz}$ was used. The lower abscissa limit is $\theta_R = 88.3°$. The upper limit is $\theta_R - \theta = 10^{-3.05°}$. The P_D distribution, of course, has both a $+f_D$ and a $-f_D$ side, corresponding respectively to the $-\theta$ and $+\theta$ sides of the $R(\theta)$ distribution. Only the $+\theta$ side of $R(\theta)$ is shown because the two sides are very similar.

The results of applying the deduced $R(\theta)$ to (3) for $\delta \simeq \delta_{min}$ are shown in Figures 5 and 6, corresponding respectively to Figures 2a and 2b. The heavy broken line is a magnification of
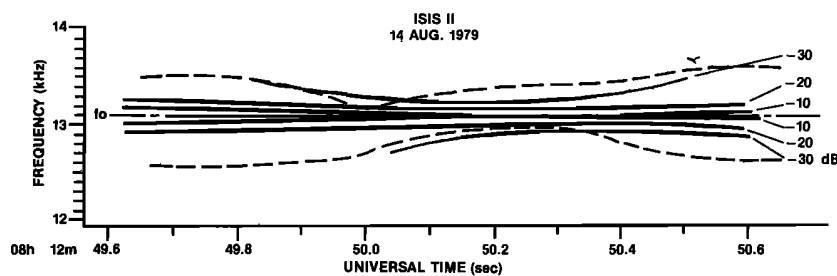

Fig. 5. Observed spectral envelope in Figure 2a (broken line) and computed contours of power levels (thin solid lines) for an all-azimuth $\vec{E}$ vector distribution having the $R(\theta)$ shown in Figure 4. The power levels in decibels are referred to the strongest signal calculated. The value $f_0 = 13.1$ kHz is the carrier frequency.
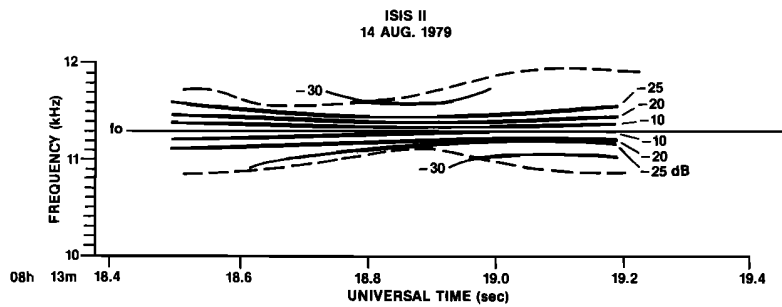
Fig. 6. Observed spectral envelope in Figure 2b (broken line) and computed contours of power levels (thin solid lines) for an all-azimuth $\bar{E}$ vector distribution having the $R(\theta)$ shown in Figure 4. The power levels in decibels are referred to the strongest signal calculated. The value $f_0 = 11.3$ kHz is the carrier frequency.

the observed signal envelopes. The solid curves are calculated contours of power levels with respect to the strongest signal in the frequency-time area covered by the plot.

The basic upturn signature can be seen by inspecting any pair of contours for a common level. For instance, in Figure 5 the -30-dB contour on the positive (upper) f_D side of f_0 is centered at about 50.2 s, while it is centered at 50.4 s on the negative (lower) side. When Figure 6 is carefully examined, it is seen that a characteristic separation of the extremum of a given $+f_D$ contour from the extremum of its $-f_D$ counterpart obtains for all contour pairs. This produces the upturn effect.

The principal result of tests with the same $R(\theta)$ at all azimuths for specific cases during the August 14 pass is the separation in time between the observed and theoretical upturn. In Figure 6 one would place the observed minimum in the upper envelope (broken line) at about 18.65 s, whereas the -30-dB contour minimum is 0.2 s later. The same holds for the other half of the pattern below the f_0 line. It was concluded that the assumption of propagation throughout all azimuths could not explain the August 14 observations.

3.3. Single Azimuth

The spectrum for the 13.1-kHz line in Figure 2a corresponding to $\delta = 90°$ was subjected to a series of tests under the assumption that all $\bar{k}$ were located in a narrow range of azimuth ϕ. The starting $P_D(f_D, \bar{L}(t_0)) = P_{max} \exp (-f_D{}^2/150^2)$ was the same as used in section 3.2. Expression (4) was used directly to calculate P_D near δ_{min}.

Better fits to the spectral envelope were obtained near δ_{min} than in section 3.2. Figure 7 shows the best fit to the observed envelope, calculated for $\bar{k}$, $\bar{E}$ vectors restricted to $\phi = -45°$ as defined by Figure A1. Apparently, the azimuthal localization of $\bar{E}$ vectors in this particular satellite orientation can very effectively discriminate against the $+f_D$ components at about 50.0 s and against $-f_D$ components about 0.25–0.35 s later.

Using the same starting P_D as for Figure 2a, the spectrum in Figure 2b was best fitted with $\phi = -45° \pm 10°$. This example was less precisely fitted to the observed signal owing to the greater signal strength which makes a thicker neck and less distinct discrimination points.

The deduced central azimuth of $\phi = -45°$ locates the wave $\bar{E}$ vectors as shown in Figure 8. This azimuthal plane is about 45° from the geographic north-south. Also, it is approximately perpendicular to the separation vector $\bar{A}$ between the OND transmitter and the foot of the field line through the spacecraft.

3.4. Importance of Parameters

The comparison of spin modulation patterns for different values of ϕ in the azimuthally restricted case showed that the time of the "upturn" signature in the spectrum is very sensitive to ϕ. Figure 9 illustrates this, showing reruns of the calculation in Figure 7 for a variety of ϕ values. These tests and the uncertainty of drawing the spectral envelope by eye indicated a total uncertainty in ϕ of about $\pm 10°$.

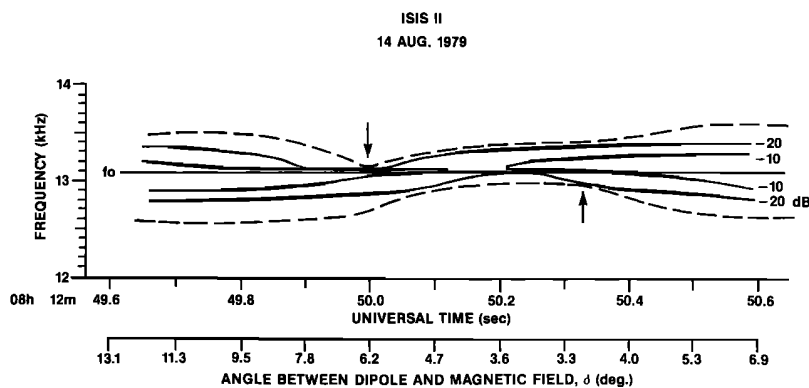The same calculation has been repeated for changes in the

Fig. 7. Observed spectral envelope in Figure 2a (broken line) and computed contours of power levels (thin solid lines) for a single-azimuth $\bar{E}$ vector distribution. The power levels in decibels are referred to the strongest signal calculated. The vertical arrows indicate times at which, first, the $+f_D$ and then the $-f_D$ components are discriminated against.
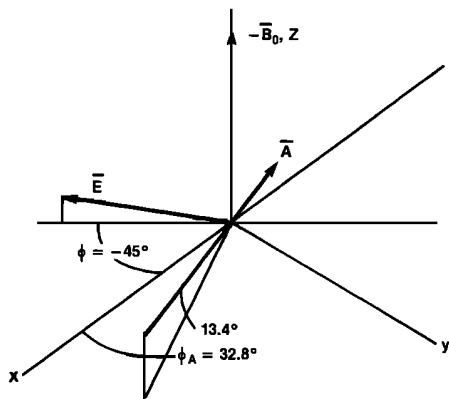
Fig. 8. Relation of the $\bar{E}$ vector, at azimuth $\phi = -45°$, to the separation vector $\bar{A}$ between the OND transmitter and the foot of the field line through the ISIS II spacecraft at 0812:50 UT on August 14, 1979.

plasma parameters: H^+ ions instead of O^+, and $f_{pe} = 0.1$ MHz instead of 0.5 MHz. Physically, these have the effect of changing θ_R by about $+0.7°$ and $-5°$, respectively. Such changes do not affect the phase of the pattern. The $+f_D$ and $-f_D$ discrimination points become a little more marked in the reduced f_{pe} case. Likewise, an increase of the assumed spectral width of P_D changes the neck thickness, except at the discrimination points. This leaves shallower and less realistic notches at the discrimination points.

Figures 4–7 were computed assuming a straight receiving dipole. Dipole bending due to differential solar heating is a source of uncertainty in this analysis. The thermal time constant of the 73-m beryllium-copper tubular dipole is 2.7 s [Mar and Garrett, 1969], compared with a spin period of about 20 s. On August 14, 1979, the spacecraft was sunlit, and the spin plane of the dipole was separated from the solar direction by approximately 20°. In the light of Vigneron's [1966] thermal steady state analysis, an examination of the

spin-sun geometry indicates that the dipole could be bowed in the time interval around $\delta = \delta_{min}$. Such an analysis predicts identical monopole shapes. Since most of the wavelengths considered here were much longer than the tip-to-tip dipole length, no dephasing of the spin pattern with respect to that calculated was expected.

The Balmain [1969] dipole theory has been used to compute the variation of the dipole impedance with the angle δ. With the effects of one species of ion included in the Balmain theory, the modulus of the impedance was found to vary by 50% for the δ change from 12° to 3.3° in Figure 7. The impedance varies more significantly for δ closer to $90° - \theta_R$, which is 1.6° in the case of Figure 7. At a given δ the change in impedance going from $f_0 + 400$ Hz to $f_0 - 400$ Hz was negligible. The modulation of the antenna impedance produced a signal modulation of 4 dB when δ changed from 12° to 3.3°. This held for all frequencies in $f_0 \pm 400$ Hz. Compared to both the observed and theoretical shapes in Figure 7, this is a gentle variation with δ and should not obscure the first-order effects of the electric vector distribution on the shape of the P_D spectrum near δ_{min}.

4. SUMMARY

A small set of examples of spin modulation on spectrally broadened pulses near 10 kHz has been examined. An azimuthally restricted $\bar{E}$ vector distribution provides a better fit to the observed spectrum than an azimuth independent set. The agreement between computed frequency-time-amplitude signatures and those observed on ISIS provides further support for the quasi-electrostatic $\bar{E}$ vector spectrum assumption.

The observational data set is limited, having been recorded for specific geophysical conditions, range of angle δ swept, and strength of the received signal. Hence it is not possible to say whether azimuthally restricted propagation occurs "normally." Precise scaling of the preferred azimuth is subject to error, arising principally from uncertainty about the shape of the receiving dipole.
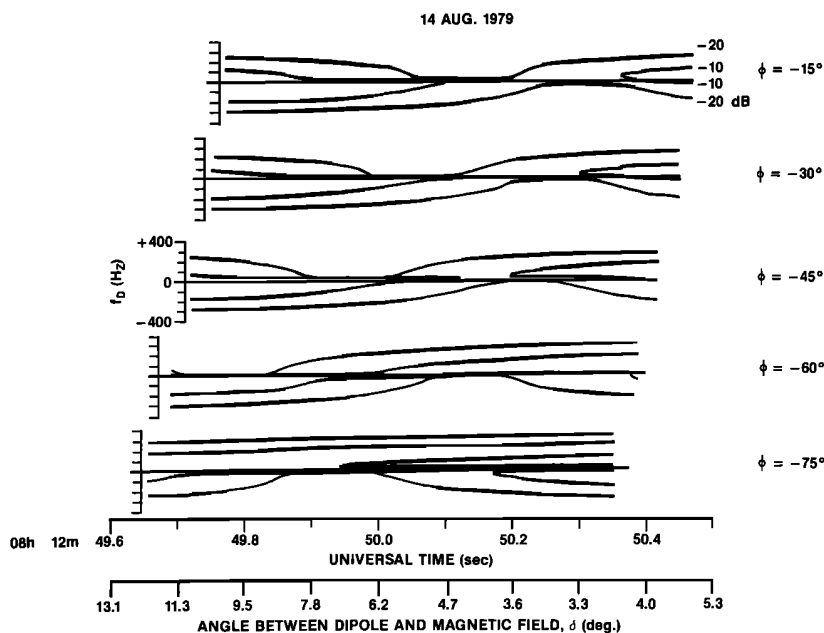

Fig. 9. Calculation of Figure 7 repeated for various values of the azimuth ϕ.

These results relate to recent theoretical proposals on VLF broadening. A scattering explanation has been advanced by *Hoc and Bell* [1985]. They assume that upgoing waves are incident upon magnetic-field-aligned slabs of enhanced or depleted ionization. The slab faces are assumed to extend many wavelengths both along and perpendicular to $\vec{B}_0$, while the slab thickness lies in the range 20–600 m. The input wave scatters coherently from the slab surfaces and produces quasi-electrostatic whistler-mode waves.

The Hoc and Bell mechanism predicts a preferred azimuth of scattering. This accords with the present deductions of a preferred azimuth. Hoc and Bell's assumption that the slabs are oriented in the magnetic east-west direction was based on the most likely orientation expected of density structure originating at auroral altitudes. Their model does not preclude the possibility of coherent scatter by slabs oriented in another direction, for instance, so as to scatter into the $\phi = -45°$ direction, as in Figure 8.

Titova et al. [1984a] proposed that longitudinal whistler-mode waves scatter nonlinearly off ionospheric ELF turbulence carried by ion acoustic waves to produce the observed resonance cone whistler-mode waves. The resulting wave spectrum is dependent upon the spectrum of the scattering irregularities. Hence *Titova et al.* [1984a] suggest that a unidirectional field-aligned current would enhance irregularities that correspond either to plus or minus Doppler components, thereby producing asymmetric $P_D(f_D)$ spectra, as observed.

The wave vector closure scheme of *Titova et al.* [1984a] would require ion waves whose wave vectors are nearly perpendicular to the magnetic field. Those authors state that field-aligned currents could be the source of such ion waves. It seems unlikely that the required perpendicular ion acoustic waves could be produced in this way in the topside ionosphere. Ion cyclotron waves, also mentioned by Titova et al., could both satisfy the k vector closure and provide the azimuthal asymmetry discussed here. Cross-field currents, being locally unidirectional, could lead to ion cyclotron waves with the required directionality.

Line broadening has been observed for a variety of transmitter-field line-spacecraft geometries [*Bell et al.*, 1983; *Bell and Hoc*, 1984; *Titova et al.*, 1984a]. Directionally biased scatterers required to produce signatures like those in Figures 2 and 3 may not always be present in the ionosphere. But when they are, it may be neccessary also that the magnetic field direction, the incident wave vector, and the effective wave vectors of the scatterers be coplanar, in order to have efficient scattering into a narrow azimuth range. The wave vectors of waves injected at the foot of the ionosphere are probably closely aligned to the vertical while propagating upward through the F region. Horizontal gradients can change the wave vector azimuth in and near the F layer [*James*, 1972]. In the case of Figure 8, these gradients could rotate the wave vector azimuth from $\phi_A + 180°$ to $-45°$. Thus the wave, emerging from the F region, would be ready to participate in the speculated linear or nonlinear scattering with scatterers whose effective wave vectors lie at $\phi = -45°$.

In conclusion, both the *Titova et al.* [1984a] and *Hoc and Bell* [1985] theories are consistent with the preferred azimuth result. The former theory has the added advantage of explaining true frequency shifts. If understanding is to advance, the next step may require better measurement of the irregularities at their subsatellite source location. This apparently

would involve simultaneous measurement at two altitudes. The $\vec{k}$ and f of the scattered whistler-mode waves would be measured at a point above the scattering region, as reported here. The $\vec{k}_i$ and f_i of the scattering ion waves would be detected at the lower height of scattering. Since $\vec{k}_i$ is speculated to be nearly perpendicular to $\vec{B}_0$, it would not be measurable by ground radars. Rather, separate rocket- or satellite-borne receiver probes would be needed.

APPENDIX

Numerical Deconvolution of a Uniform Azimuthal Distribution of $R(\theta)$ From Observed P_D

In principle, equation (3) can be inverted to find the distribution $R(\theta)$. First, note that θ and ϕ are related through the definition of the Doppler frequency

$$f_D = -\vec{k} \cdot \vec{v}/2\pi = -v(\eta_x \sin \theta \cos \phi + \eta_z \cos \theta) f_0 n(\theta)/c \quad (A1)$$

In Figure A1, θ and ϕ are angles that specify the $\vec{k}$ direction, and η_x and η_z are the direction cosines of $\vec{v}$, defined to lie in the x-z plane. Because this discussion deals only with upgoing waves, with either positive or negative Doppler, it was found convenient to assign the angles θ and ϕ to the ranges $-\theta_R \le \theta \le \theta_R$ and $-90° \le \phi \le 90°$. The value f_0 is the carrier frequency and c the speed of light.

Two steps have been taken which simplify the computation. The formula (A1) establishes the range of θ corresponding to the assumed range of ϕ. Because we wish to consider all ϕ in $-90°$ to $+90°$, there are some azimuths that require a very large $n(\theta)$ to satisfy a given f_D value. The first simplification therefore is to limit the $n(\theta)$ values to those with negligible Landau and cyclotron damping. In an equilibrium hot plasma having $T \simeq 2000$ K this means that $n(\theta) \le 1000$ and $|f_D| \le 400$ Hz.

The second simplification is to assume that R has no ϕ dependence. For numerical deconvolution the same $R(\theta)$ distribution is assumed valid throughout the entire range $-90° \le \phi \le +90°$. In this simplified case, we are concerned with inverting the following discrete summation form of (3):

$$P_D(f_D, \vec{L}) = C \sum_j K(\theta_j, \phi_j, \vec{L}, \vec{v}) R(\theta_j)(\Delta\phi)_j \quad (A2)$$

where K is the fractional part of the integrand in (3). The deconvolution starts with the solution set ($f_D = 400$ Hz, $\phi_0 = 0$, $\theta = \theta_0$) of (A1). It is assumed that $R(\theta_0) = 0$, corresponding to $P_D(400, \vec{L}) = 0$.

Next, a step downward in f_D is taken to f_{D_1}. The solution sets (f_{D_1}, ϕ_1, θ_0) and (f_{D_1}, ϕ_0, θ_1) are found from (A1). Then $R(\theta_1)$ is determined from

$$P_D(f_{D_1}, \vec{L}) = 2CK(\phi_0, \theta_1)R(\theta_1)(\phi_1 - \phi_0) \quad (A3)$$

where, henceforth, the constant arguments $\vec{L}$ and $\vec{v}$ are understood in K. The factor 2 arises from the contributions from the $\phi < 0$ and $\phi > 0$ quadrants. These happen to be equal in this first step because K is evaluated at $\phi = \phi_0 = 0$ for both.

Another step downward is taken to f_{D_2}. The sets (f_{D_2}, ϕ_2, θ_0), (f_{D_2}, ϕ_1, θ_1), and (f_{D_2}, ϕ_0, θ_2) are found from (A1). Now

$$P_D(f_{D_2}) = 2CK(\phi_0, \theta_2)R(\theta_2)(\phi_1 - \phi_0)$$

$$+ CK(\phi_1, \theta_1)R(\theta_1)(\phi_2 - \phi_1) + CK(-\phi_1, \theta_1)R(\theta_1)(\phi_2 - \phi_1)$$

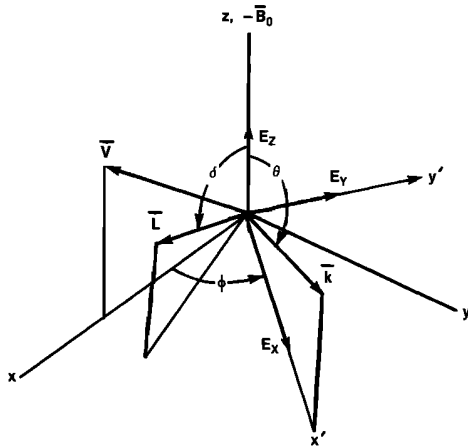allows $R(\theta_2)$ to be determined. At this step the contributions

Fig. A1. Coordinate axes and principal vectors. The spacecraft velocity $\bar{v}$ is in the x-z plane. The variables θ and ϕ are respectively the polar and azimuthal angles of the wave vector $\bar{k}$. $\bar{L}$ is the antenna direction and x' and y' are rotated axes for computation of E.

associated with the new θ_2 from the two quadrants are different.

The deconvolution proceeds, each step adding a θ and $R(\theta)$ pair to the lengthening set of θ and $R(\theta)$ on which the succeeding iteration will be based. In general,

$$R(\theta_m) = \left\{ P_D(f_{Dm}) - C \sum_{j=1}^{m-1} [\{K(\phi_{m-j}, \theta_j) + K(-\phi_{m-j}, \theta_j)\} \right.$$
$$\left. \cdot R(\theta_j)(\phi_{m-j+1} - \phi_{m-j})] \right\} [2CK(\phi_0, \theta_m)\phi_1]^{-1} \qquad (A4)$$

This procedure results in the $R(\theta)$ distribution for whichever side of the $P_D(f_D)$ spectrum is being analyzed. If desired, the opposite side can be similarly treated and the resulting $R(\theta)$ compared with that obtained in the first deconvolution.

Multiplicative Factor for Waves
Confined to One Azimuth

The factor F_D developed by *Bell et al.* [1983] is evaluated using the geometry shown in Figure A1. Because of the more general geometry used here, we seek

$$F_D = (\bar{l} \cdot \bar{e}_{Re})^2 + (\bar{l} \cdot \bar{e}_{Im})^2$$

in which we add the squares of the real (Re) and imaginary (Im) voltage contributions from the $\bar{E}$ field polarization ellipse. The variables $\bar{l}$ and $\bar{e}$ are unit vectors of $\bar{L}$ and $\bar{E}$, respectively.

First, with reference to the coordinate system $x' - y' - z$ in Figure A1, the direction cosines of $\bar{E}$ have been derived by *Bell et al.* [1983]. Referred now to the x-y-z axes in Figure A1, the antenna cosines are $\bar{l} = (\beta_x, \beta_y, \beta_z)$. Then

$$\bar{l} \cdot \bar{e}_{Re} = \beta_x \gamma_x \cos \phi + \beta_y \gamma_x \sin \phi + \beta_z \gamma_z$$

$$\bar{l} \cdot \bar{e}_{Im} = -\beta_x \gamma_y \sin \phi + \beta_y \gamma_y \cos \phi$$

The reference orientation is $\bar{l} = (\beta_{x\perp}, \beta_{y\perp}, 0)$ where the subscript "$\perp$" indicates the perpendicular case, $\delta = 90°$ at $t = t_0$. Thus the ratio of F_D required in (4) is

$$\frac{F_D(\theta, \bar{L}(t), \phi)}{F_D(\theta, \bar{L}(t_0), \phi)} = [(\beta_x \gamma_x \cos \phi + \beta_y \gamma_x \sin \phi + \beta_z \gamma_z)^2$$

$$+ \gamma_y^2 (-\beta_x \sin \phi + \beta_y \cos \phi)^2][\gamma_x^2 (\beta_{x\perp} \cos \phi + \beta_{y\perp} \sin \phi)^2$$

$$+ \gamma_y^2 (-\beta_{x\perp} \sin \phi + \beta_{y\perp} \cos \phi)^2]^{-1} \qquad (A5)$$

REFERENCES

Balmain, K. G., Dipole admittance for magnetoplasma diagnostics, *IEEE Trans. Antennas Propag.*, *AP-17*(3), 389–392, 1969.

Bell, T. F., and N. D. Hoc, The spectral broadening of VLF transmitter signals on magnetic field lines in the inner radiation belt, *Eos Trans. AGU*, *65*, 1061, 1984.

Bell, T. F., H. G. James, U. S. Inan, and J. P. Katsufrakis, The apparent spectral broadening of VLF transmitter signals during transionospheric propagation, *J. Geophys. Res.*, *88*(A6), 4813–4840, 1983.

Bell, T. F., J. P. Katsufrakis, and H. G. James, A new type of VLF emissions triggered at low altitude in the subauroral region by Siple Station VLF transmitter signals, *J. Geophys. Res.*, *90*(A12), 12,183–12,194, 1985.

Franklin, C. A., T. Nishizaki, and W. E. Mather, A wideband VLF receiver for the Alouette II and ISIS-A satellites, *Def. Res. Telecommun. Estab. Tech. Memo 522*, Dep. of Natl. Def., Ottawa, Ont., Canada, 1968.

Hoc, N. D., and T. F. Bell, Quasi-electrostatic waves excited during the scattering of coherent whistler mode waves from magnetic field aligned plasma density irregularities, *Eos Trans. AGU*, *66*(46), 1038–1039, 1985.

Inan, U. S., and T. F. Bell, Spectral broadening of VLF transmitter signals observed on DE-1: A quasi-electrostatic phenomenon?, *J. Geophys. Res.*, *90*(A2), 1771–1775, 1985.

International Association of Geomagnetism and Aeronomy, Division I, Working Group 1, International geomagnetic reference field revision 1985, *Eos Trans. AGU*, *67*(24), 523–524, 1986.

James, H. G., Refraction of whistler-mode waves by large-scale gradients in the middle-latitude ionosphere, *Ann. Geophys. 28*(2), 301–339, 1972.

Mar, J., and T. Garrett, Mechanical design and dynamics of the Alouette spacecraft, *Proc. IEEE*, *57*(6), 882–896, 1969.

McDiarmid, I. B., J. R. Burrows, and M. D. Wilson, Comparison of magnetic field perturbations at high latitudes with charged particle and IMF measurements, *J. Geophys. Res.*, *83*(A2), 681–688, 1978.

Tanaka, Y., M. Hayakawa, D. Lagoutte, and F. Lefeuvre, Study of the middle latitude broadening of the spectrum of the waves emitted from the ground, paper presented at the Conference on the Results of the ARCAD-3 Project and of the Recent Programmes in Magnetospheric and Ionospheric Physics, Toulouse, Cent. Natl. de la Rech. Sci., Paris, May 22–25, 1984.

Titova, E. E., V. I. Di, V. E. Yurov, O. M. Raspopov, V. Yu. Trakhtengertz, F. Jiricek, and P. Triska, Interaction between VLF waves and the turbulent ionosphere, *Geophys. Res. Lett.*, *11*(4), 323–326, 1984a.

Titova, E., V. Yurov, A. Perlikov, O. Raspopov, V. Trakhtengertz, O. Maltseva, O. Molchanov, and Y. Galperin, On the spectral broadening of ground transmitters VLF-signals in the high latitude ionosphere observed from INTERCOSMOS-19 and AUREOL-3 satellites, paper presented at the Conference on the Results of the ARCAD-3 Project and of the Recent Programmes in Magnetospheric and Ionospheric Physics, Toulouse, Cent. Natl. de la Rech. Sci., Paris, May 22–25, 1984b.

Titova, E. E., F. Irzhichek, I. V. Lychkina, O. M. Raspopov, V. Yu. Trakhtengerts, P. Triska, and V. E. Yurov, Spectral broadening of signals from VLF transmitters in the upper ionosphere, *Geomagn. Aeron.*, *24*(6), 770–776, 1984c.

Vigneron, F. R., Transient temperature and thermal curvature behavior of sounder antennas on Alouette satellites, *Def. Res. Telecommun. Estab. Rep. 1167*, Def. Res. Board, Ottawa, Ont., Canada, 1966.

T. F. Bell, Space, Telecommunications and Radioscience Laboratory, Stanford University, Stanford, CA 94305.

H. G. James, Communications Research Centre, Shirley Bay, P.O. Box 11490, Station H, Ottawa, Ontario, Canada K2H 8S2.